A mixing-length formulation for the turbulent Prandtl number in wall-bounded flows with bed roughness and elevated scalar sources

John P. Crimaldi[a)]
Department of Civil, Environmental, and Architectural Engineering, University of Colorado, Boulder, Colorado 80309-0428

Jeffrey R. Koseff and Stephen G. Monismith
Department of Civil and Environmental Engineering, Stanford University, Stanford, California 94305-4020

(Received 7 November 2005; accepted 20 June 2006; published online 5 September 2006)

Turbulent Prandtl number distributions are measured in a laboratory boundary layer flow with bed roughness, active blowing and sucking, and scalar injection near the bed. The distributions are significantly larger than unity, even at large distances from the wall, in apparent conflict with the Reynolds analogy. An analytical model is developed for the turbulent Prandtl number, formulated as the ratio of momentum and scalar mixing length distributions. The model is successful at predicting the measured turbulent Prandtl number behavior. Large deviations from unity are shown in this case to be consistent with measurable differences in the origins of the momentum and scalar mixing length distributions. Furthermore, these deviations are shown to be consistent with the Reynolds analogy when the definition of the turbulent Prandtl number is modified to include the effect of separate mixing length origin locations. The results indicate that the turbulent Prandtl number for flows over complex boundaries can be modeled based on simple knowledge of the geometric and kinematic nature of the momentum and scalar boundary conditions. © *2006 American Institute of Physics*. [DOI: 10.1063/1.2227005]

I. INTRODUCTION

The transport of mass or heat within turbulent flows is a fundamental physical process in many natural and engineered systems. Historically, engineering approaches to modeling such systems employed a turbulence closure scheme for the momentum field based on either an eddy viscosity or a mixing length formulation. The calculation of the scalar transport then often made use of the so-called Reynolds analogy, whereby the scalar dispersivity was assumed to be proportional to the eddy viscosity. The constant of proportionality, the turbulent Prandtl number $\mathrm{Pr_t}$, was assumed to be close to unity. The shortcomings of this approach (especially in complex flows) are now well known, and this simple model has been replaced with more advanced ones, where $\mathrm{Pr_t}$ may not explicitly appear. Nonetheless, the hypothetical concept of momentum and scalar mixing lengths, and their ratio ($\mathrm{Pr_t}$) endures in the literature and remains useful for the description of some systems.

Numerous studies have measured or calculated $\mathrm{Pr_t}$ near solid boundaries; see reviews by Reynolds[1] and Kays.[2] Analytical studies,[3] direct numerical simulations (DNS),[4,5] and experiments[6,7] all suggest that $\mathrm{Pr_t}$ has a value between 0.85 and unity in the logarithmic region of the boundary layer, in reasonable agreement with the Reynolds analogy. Larger values for $\mathrm{Pr_t}$ have been predicted in the viscous sublayer ($z^+ < 5$) due to the dramatic local decrease in eddy diffusivity.[3,5] Similarly, values of $\mathrm{Pr_t}$ as large as 4 have been measured for heat flux and vapor flux above plant canopies.[8] For flows over rough surfaces, the nature of the roughness has been shown to only slightly alter $\mathrm{Pr_t}$.[9]

Many turbulent flows of interest develop in the presence of a solid boundary. The boundary acts as a source or sink for momentum in the overlaying fluid, and turbulence enhances this boundary momentum flux. In the case of a rough boundary, the momentum sink is distributed continuously between the roughness "peaks and valleys," with an effective sink location somewhere in between. Scalar quantities may also flux across the boundary. In many cases, the source or sink of momentum and of the scalar are colocated, such as in the case of a heated or porous wall. However, there are other cases where the scalar is introduced near the wall in such a way that it does not directly coincide with the range of heights that are responsible for the momentum sink. For example, in large-scale flows over urban environments or forests, momentum is interacting with the boundary over the entire range of building or tree heights, but a scalar might be added or removed only from specific height (e.g., the rooftop or within the vegetated canopy). And in boundary layer applications, scalars may be introduced via blowing such that the effective scalar source location differs from that of the solid wall. In these cases, the Reynolds analogy breaks down close to the boundary and the turbulent Prandtl number can deviate significantly from unity. We describe a case study of such a situation in a channel flow where the sinks and sources of momentum and scalar are not colocated, and we present an analysis that enables the near-bed turbulent Prandtl number to be predicted based on the flow conditions and the geometry of the problem.

The turbulent Prandtl number is a measure of the relative

a)Electronic mail: crimaldi@colorado.edu

rates of mixing of the momentum and scalar quantities at a given location in the flow. When Pr_t is large, momentum is being transported by the turbulence more actively than the scalar quantity. However, this difference in relative transport or mixing rates need not be only due to fundamental difference in the way the flow transports scalars as compared to momentum. The results of this study suggest that the large Pr_t values measured near the bed can be almost completely accounted for by the fact that the momentum and scalar fields have origins that are spatially separated; furthermore, the difference in the locations of the origins is related most specifically to the geometry of the boundary conditions rather than to the turbulence itself. We argue that the *intrinsic* relative ability of turbulence to transport momentum versus scalars is governed by a parameter that we call the intrinsic turbulent Prandtl number, $\widetilde{Pr}_t$. The data suggest that while Pr_t can vary greatly, $\widetilde{Pr}_t$ is of order unity.

The data used in this study were acquired by the authors as part of an investigation of the interactions between a turbulent boundary layer flow and the feeding currents of a model population of filter-feeding bivalves (specifically, the Asian clam *Potamocorbula amurensis*). *P. amurensis* is an introduced species that has proliferated throughout San Francisco Bay, and is thought to serve as a control on the population dynamics of suspended phytoplankton.[10] The clams ingest phytoplankton-laden fluid from the flow above them through an in-current siphon, filter the phytoplankton, and expel phytoplankton-depleted fluid back into the flow through an ex-current siphon. The extent to which beds of bivalves can filter the full vertical extent of the water column depends on the magnitude and distribution of vertical mixing in the flow. An earlier study[11] examined the perturbation effect of the in-current and ex-current flows on vertical mixing in the benthic boundary layer. Ex-current flows from an array of model clams in a laboratory flume were marked with a known concentration of dye (representing phytoplankton depletion), and scalar fluxes were calculated from simultaneous measurements of velocity and concentration.

In the present study, we use data from the previous physical-biological study and focus on the physics associated with scalar mixing within a turbulent boundary layer. In particular, we examine the vertical distribution of the turbulent Prandtl number, and develop a model for the distribution based on a mixing-length formulation.

II. DESCRIPTION OF EXPERIMENTS

A. Flow facility and siphon models

The experiments were performed in an open-channel, recirculating flume with a 3 m test section. Water is pumped into a constant-head tank, and then enters the upstream end of the flume through a diffuser, passes through three sets of homogenizing screens, and accelerates through a 6.25:1 two-dimensional contraction section before entering the 0.6 m wide channel that leads to the test section. A 3 mm rod spans the bed at the channel entrance to trip the turbulent boundary layer. The turbulence structure within the momentum boundary layer, measured with a laser-Doppler velocimeter (LDV)

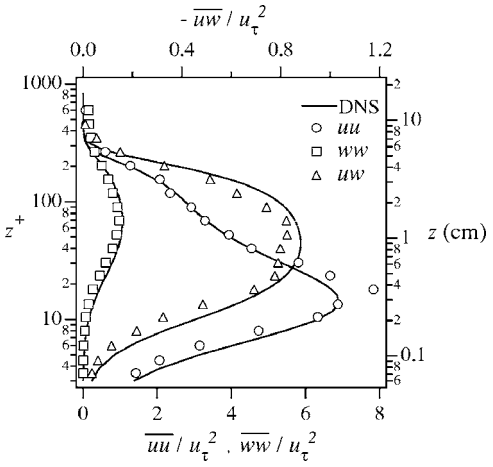

FIG. 1. Normalized turbulence intensities and Reynolds stresses from LDV data (symbols, Re_θ=1320) and DNS (solid lines, Re_θ=1410). LDV data from flume flow over a smooth bed, with free-stream velocity U_0=11.6 cm/s. DNS data from Spalart (Ref. 12).

over a smooth bed, agrees well with direct numerical simulations (DNS) at similar Reynolds numbers by Spalart,[12] as shown in Fig. 1.

An array of model clam siphons was developed[11,13,14] to investigate the role of in-current and ex-current siphon currents, siphon roughness, and siphon filtration on the turbulent momentum and scalar fields above the bed. The array of siphons runs lengthwise down the center of the bed of the flume test section, as shown in Fig. 2. Two types of model clams were used in this study: one with raised siphons [Fig. 3(a)] and one with flush siphons [Fig. 3(b)]. Each model clam consists of a pair of siphons: a 3.2 mm inside diameter in-current siphon that draws ambient fluid from above at a steady flow rate, and a 1.6 mm inside diameter ex-current siphon that expels fluid into the overlaying flow at the same volumetric flow rate as the in-current siphon. Following Monismith *et al.*,[15] we assumed a continuous and constant flow rate through the siphons (although the flow rate was varied from experiment to experiment). For the raised-siphon models, the siphon exits are 3.2 mm above the bed, and the siphons form roughness elements. For the flush siphons, the bed is smooth, but perforated with the siphon holes. For both

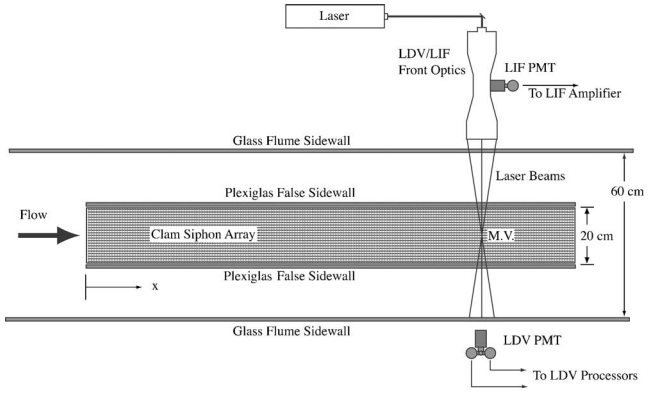

FIG. 2. Top view of the flume test section and the LDV/LIF instrumentation.

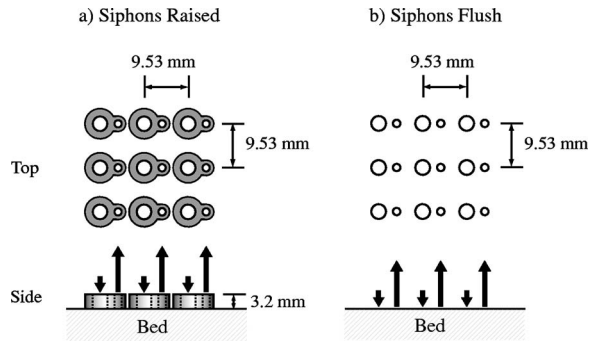

FIG. 3. Top and side views of sample 3×3 array of raised (a) and flush (b) model clam siphons. The mean flume flow is from left to right. The arrows indicate the direction and relative velocity of the ex-current (upward) and in-current (downward) flows. The inside diameters of the ex-current and in-current siphons are $d_e=1.6$ mm and $d_i=3.2$ mm, respectively. A 21×189 array of clam siphons encompassing an area 0.2 m $\times$ 1.8 m was used in the experiments.

types, 3969 siphon pairs are arranged in a 21×189 array, with the geometry shown in Fig. 3. To simulate filtration, the in-current flows are removed from the test section and disposed of, while the ex-current flows are dosed with a known concentration of dye (thus, the dye labels fluid that has been filtered, and clear water represents unfiltered fluid).

B. Instrumentation

Measurements of turbulent velocity and scalar concentration were made using a combined LDV and laser-induced fluorescence (LIF) probe. Related techniques have been used in previous studies to measure turbulent transport in jets and plumes.[16–19] The combined LDV/LIF probe used in the present study is based on a DANTEC 2-D LDV system, with the LDV receiving optics and photomultiplier tube (PMT) placed in the forward-scatter location, as shown in Fig. 2. This positioning for the LDV PMT takes advantage of the strong forward-scatter lobes associated with Mie particle scattering, resulting in a stronger signal-to-noise ratio for the LDV relative to a backscatter approach. The disadvantage is that the receiving optics must be repositioned each time the LDV is moved to a new measurement location. The LDV is driven with an argon-ion laser, operating at a nominal power of 1 W, in a single-line mode at 514.5 nm. The LDV optics split the laser into three beams, which are focused through a 310 mm lens to form a measuring volume within the flow. The dimensions of the measuring volume were approximately 0.1 mm in the vertical and streamwise directions, and 1 mm in the cross-channel direction. A 514.5 nm notch filter allows laser light scattered from particles in the flow to enter the LDV PMT, but blocks stray light and fluoresced light.

The LIF system uses the high-intensity laser light in the LDV measurement volume as an excitation source for fluorescent dye introduced into the flow in the ex-current streams. Rhodamine 6G was used as the dye, based on its relatively low toxicity and low susceptibility to photobleaching.[20] Some commonly used dyes (e.g., fluorescein) are highly susceptible to photobleaching, which introduces a correlation between the LIF measurements and the flow velocity, which is undesirable when scalar flux measurements are being made. Dye passing through the measurement volume fluoresces in an omnidirectional pattern. The LIF receiving optics can therefore be placed in a backscatter location without any loss of signal strength. The PMT for the LIF system was placed in a backscatter section within the LDV transmission optics. A pinhole mask in the backscatter optics was used to block light that did not originate within the measurement volume, and a 555 nm notch filter was used to block light outside the emission spectrum of Rhodamine 6G.

C. Experimental conditions

Three quantities were varied in the experiments: the siphon height h, the siphon flow rate Q, and the free-stream flow velocity U_0. Two siphon heights were tested, $h=3.2$ mm ("raised") and $h=0$ mm ("flush"). For each of the two siphon heights, permutations of four values of Q (0, 0.030, 0.045, and 0.060 ml/s) and U_0 (10, 20, 30, and 40 cm/s) were tested, resulting in a total of 32 experimental runs. For each of the 32 conditions, data were taken at 20 logarithmically spaced vertical stations. At each station, 100 000 simultaneous samples of concentration and velocity were acquired at approximately 80 Hz. The dimensional variables Q and U_0 can be combined into a single dimensionless parameter,[13] defined as the ratio of the average ex-current jet velocity $\overline{W_e}$ and the free-stream velocity U_0:

$$\mathrm{VR}=\overline{W_e}/U_0, \tag{1}$$

where

$$\overline{W_e}=\frac{Q}{\pi d_e^2/4}. \tag{2}$$

For our experiments, VR ranges from 0 to 0.3. For each experimental case, the shear velocity u_τ was determined using a fit of the mean streamwise velocity data to the law of the wall. Depending on the value of h and Q, the value of u_τ was between 3.8% and 5.0% of U_0.

III. ANALYTICAL METHODOLOGY

A. Momentum mixing lengths

We begin with the Reynolds stress model proposed by Prandtl based on the concept of a hypothetical "mixing length." This model relates the Reynolds stress to the mean velocity gradient through the relationship

$$\overline{uw}=-\ell_M^2\left|\frac{\partial U}{\partial z}\right|\frac{\partial U}{\partial z}, \tag{3}$$

where ℓ_M is an assumed mixing length of momentum. This model can be used to form a general law of the wall, which applies over the entire inner layer:

$$\frac{\partial U^+}{\partial z^+}=\frac{1}{2\ell_M^{+2}}\left(\sqrt{1+4\ell_M^{+2}}-1\right). \tag{4}$$

Van Driest[21] proposed a momentum mixing length distribution given by

$$\ell_M^+ = \kappa z^+ \left[1 - \exp\left(\frac{-z^+}{26} \right) \right]. \tag{5}$$

This damped mixing length distribution modifies the near-wall momentum mixing lengths so that Eq. (4) integrates to $U^+ = z^+$ in the viscous sublayer. Farther from the wall, in the log layer, the mixing length distribution reverts to the linear form

$$\ell_M^+ = \kappa z^+. \tag{6}$$

We now consider flow over a rough boundary. The geometry of the roughness elements introduces an additional set of length scales that are needed to completely describe the effects of the roughness on the flow.[8] However, the roughness Reynolds number, given by

$$h^+ = \frac{h u_\tau}{\nu}, \tag{7}$$

is a useful single parameter for describing the resulting behavior of the flow based on the ratio of a typical roughness element height (a single length scale) to the viscous length scale ν/u_τ. Flows where $h^+ < h_S^+$, where $h_S^+ \approx 5$, are said to be dynamically smooth since the roughness elements reside completely within the viscous sublayer and do not disturb the flow. For flows where $h^+ > h_R^+$, where $h_R^+ \approx 60$, the disturbances completely erode the viscous sublayer, and the log law extends all the way to the point where the mean velocity is zero (usually somewhere between $z=0$ and $z=h$); the flow in this case is said to be fully rough. For flows where $h_S^+ < h^+ < h_R^+$, the roughness elements protrude through the viscous sublayer and disturb the overlaying flow; these flows are said to be transitionally rough. The extent of the disturbance in the transitionally rough regime can be parametrized in terms of h^+.

We introduced a modification to the Van Driest mixing length to account for the effect of roughness in the transitionally rough regime. The new mixing length distribution is given by

$$\ell_M^+(z^+,h^+) = \kappa z^+ \widetilde{D}(z^+,h^+), \tag{8}$$

where

$$\widetilde{D}(z^+,h^+) = 1 - \left[\frac{h_R^+ - h^+}{h_R^+ - h_S^+} \exp\left(\frac{-z^+}{26} \right) \right] \quad \text{for } h_S^+ \le h^+ \le h_R^+. \tag{9}$$

When $h^+ = h_S^+$, Eq. (8) matches Eq. (5), which is used for $h^+ < h_S^+$. When $h^+ = h_R^+$, Eq. (8) matches Eq. (6), which is used for $h^+ > h_R^+$. For intermediate values of h, Eq. (9) applies a linear interpolation of the Van Driest exponential damping factor, where a linear interpolation is chosen for simplicity. Figure 4 shows the assumed momentum mixing length distribution $\ell_M^+(z^+,h^+)$ for the two limiting and one intermediate roughness Reynolds number values.

Because $\ell_M^+(z^+,h^+)$ is dependent not only on the distance from the wall but also on the value of the roughness

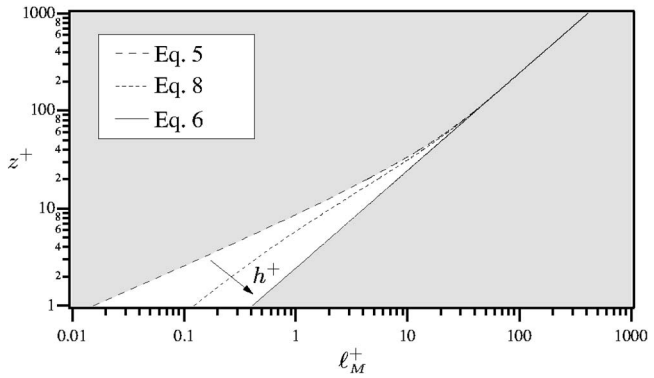

FIG. 4. Assumed mixing-length distribution ℓ_M^+ for a range of values of h^+. The arrow shows the direction of increasing h^+. Equation (5) is used for $h^+ \le h_S^+$, Eq. (6) is used for $h^+ \ge h_R^+$, and Eq. (8) is used for intermediate h^+ values ($h^+ = 20$ is shown).

Reynolds number, it is convenient to define a Reynolds-number-independent momentum mixing length, $\widetilde{\ell_M^+}(z^+)$, given by

$$\widetilde{\ell_M^+}(z^+) = \frac{\ell_M^+(z^+,h^+)}{\widetilde{D}(z^+,h^+)} = \kappa z^+. \tag{10}$$

Equation (10) removes the effect of the roughness Reynolds number from the momentum mixing length equation—all mixing length distributions expressed in this form map back onto the straight line $\widetilde{\ell_M^+} = \kappa z^+$, regardless of the value of h^+. This formulation will simplify the analysis developed in later sections.

B. Scalar mixing lengths and Pr_t

The behavior of the vertical scalar flux $\overline{wc}$ can also be modeled in terms of mixing lengths. A scalar mixing length can be defined through the relationship

$$\overline{wc} = -\ell_M \frac{\partial U}{\partial z} \ell_C \frac{\partial C}{\partial z}, \tag{11}$$

where ℓ_C is the scalar mixing length. Combining Eqs. (11) and (3) gives the turbulent Prandtl number

$$\mathrm{Pr_t} \equiv \frac{\ell_M}{\ell_C} = \frac{\overline{uw} \big/ \left(\partial U / \partial z \right)}{\overline{wc} \big/ \left(\partial C / \partial z \right)}, \tag{12}$$

which can be combined with Eq. (8) to give

$$\ell_C^+(z^+,h^+) = \mathrm{Pr_t^{-1}}\, \kappa z^+ \widetilde{D}(z^+,h^+), \tag{13}$$

where $\ell_C^+ = \ell_C u_\tau / \nu$ is the nondimensional scalar mixing length. Because $\ell_C^+(z^+,h^+)$ is dependent on the value of the roughness Reynolds number, it is again convenient to define a Reynolds-number-independent scalar mixing length $\widetilde{\ell_C^+}(z^+)$, given by

$$\widetilde{\ell_C^+} = \frac{\ell_C^+(z^+,h^+)}{\widetilde{D}(z^+,h^+)}, \tag{14}$$

which, when combined with Eq. (13), gives

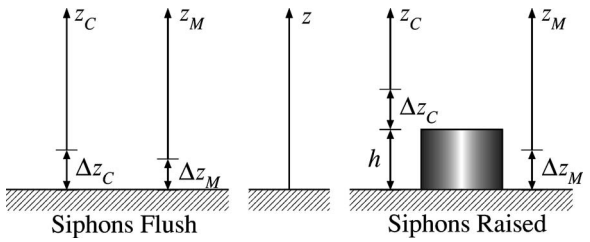

FIG. 5. A definition of the vertical coordinates for flush (left) and raised (right) siphons.

$$\widetilde{\ell_C^+}(z^+) = \mathrm{Pr}_t^{-1}\kappa z^+. \tag{15}$$

Equation (15) removes the effect of the roughness Reynolds number from the scalar mixing length equation—all mixing length distributions expressed in this form conveniently map back onto the straight line $\widetilde{\ell_C^+}=\mathrm{Pr}_t^{-1}\kappa z^+$, regardless of the value of h^+.

C. Mixing length origins

The assumed momentum and scalar mixing length distributions given by Eqs. (10) and (15) were formulated under the assumption that both the momentum and scalar mixing lengths vanish at identically $z=0$. This is likely to be a good assumption only if the momentum sink and the scalar source are located identically at $z=0$. For example, a smooth heated plate can be considered both a momentum sink as well as a scalar (heat) source located at $z=0$; there is no mechanism by which the plate can introduce or remove momentum or scalars anywhere other than at the boundary.

By way of contrast, consider the more complicated flow boundary associated with the siphons used in the present study, as shown in Fig. 5. The siphons are roughness elements with height h, where $h=0$ for the flush siphon array. The roughness elements extract momentum from the flow over a distributed vertical extent over the range $0\leq z\leq h$. Far from the bed, however, it is reasonable to model the roughness as a momentum extraction occurring at a discrete vertical location $z=\Delta z_M$. The scalar dye is introduced into the flow from the top of the siphons (i.e., at $z=0$ for the flush siphons and at $z=h$ for the raised siphons). The scalar is injected into the flow with some vertical momentum, causing it to mix into the flow over a distributed vertical range. Far from the wall, this scalar injection can be modeled as a momentumless scalar source occurring at a discrete vertical location $z=h+\Delta z_C$.

We define two separate coordinate systems, z_M and z_C, for the momentum and scalar fields, respectively. The two coordinate systems are related to the base coordinate z as

$$z_M = z - \Delta z_M, \tag{16}$$

$$z_C = z - (h + \Delta z_C). \tag{17}$$

The offset parameters Δz_M and Δz_C define the distances from the wall at which the boundary momentum sink and scalar sources would be located if they were assumed to act at a discrete vertical location rather than over a distributed range.

D. A model for Pr_t based on Δz_M and Δz_C

We now present a conceptual model for the turbulent Prandtl based on the distribution of momentum and scalar mixing lengths, allowing that these two distributions may have separate origins. Our model defines Pr_t in the usual way as the ratio of the momentum mixing length to the scalar mixing length. To eliminate the effect of roughness Reynolds number in our formulation, we use Eqs. (10) and (15) to rewrite Eq. (12) as

$$\mathrm{Pr}_t(z_C^+) = \frac{\widetilde{\ell_M^+}(z_C^+)}{\widetilde{\ell_C^+}(z_C^+)}. \tag{18}$$

As discussed earlier, the $\widetilde{\ell_M^+}$ and $\widetilde{\ell_C^+}$ distributions are always linear, regardless of the roughness Reynolds number. We introduce a new parameter, $\widetilde{\mathrm{Pr}}_t$, that we call the *intrinsic* turbulent Prandtl number. This parameter is defined as

$$\widetilde{\mathrm{Pr}}_t = \frac{\partial \ell_M}{\partial z} \Big/ \frac{\partial \ell_C}{\partial z} = \frac{\partial \widetilde{\ell_M^+}}{\partial z_M^+} \Big/ \frac{\partial \widetilde{\ell_C^+}}{\partial z_C^+}. \tag{19}$$

By defining $\widetilde{\mathrm{Pr}}_t$ in terms of mixing length derivatives, we remove the effect of the mixing length origin location and focus on the vertical growth rate. Note that $\widetilde{\mathrm{Pr}}_t=\mathrm{Pr}_t$ only if the momentum and scalar mixing length origins are both at $z=0$ (i.e., $\Delta z_M=0$ and $\Delta z_C=0$). As an alternative to defining $\widetilde{\mathrm{Pr}}_t$ in terms of mixing length derivatives, it can be defined in terms of a ratio of the mixing length distributions themselves, but evaluated at separate locations:

$$\widetilde{\mathrm{Pr}}_t(z_C^+) = \frac{\widetilde{\ell_M^+}(z_M^+)}{\widetilde{\ell_C^+}(z_C^+)}. \tag{20}$$

The momentum mixing length distribution in the model is based on Eq. (6), but written in terms of z_M instead of z, allowing for a mixing length origin that is not at the wall. Using Eq. (10) to remove the effect of the roughness Reynolds number, our model momentum mixing length distribution is then

$$\widetilde{\ell_M^+} = \kappa(z - \Delta z_M)^+ = \kappa z_M^+. \tag{21}$$

Likewise, the scalar mixing length distribution is based on Eq. (15), but written in terms of z_C instead of z. Furthermore, the turbulent Prandtl number Pr_t is replaced by $\widetilde{\mathrm{Pr}}_t$, allowing a more meaningful comparison between two linear distributions with separate origins:

$$\widetilde{\ell_C^+} = \widetilde{\mathrm{Pr}}_t^{-1}\kappa[z - (h + \Delta z_C)]^+ = \widetilde{\mathrm{Pr}}_t^{-1}\,\kappa z_C^+. \tag{22}$$

Combining Eqs. (16)–(18), (21), and (22) gives the following model for Pr_t:

$$\mathrm{Pr}_t(z_C) = \frac{\widetilde{\ell_M^+}}{\widetilde{\ell_C^+}} = \widetilde{\mathrm{Pr}}_t\frac{z_M^+}{z_C^+} = \widetilde{\mathrm{Pr}}_t\left(1 + \frac{\Delta\ell^+}{z_C^+}\right), \tag{23}$$

where $\Delta\ell^+$ is the distance between the momentum and scalar mixing length origins in terms of viscous wall units:

$$\Delta\ell^+ = h^+ + \Delta z_C^+ - \Delta z_M^+. \tag{24}$$

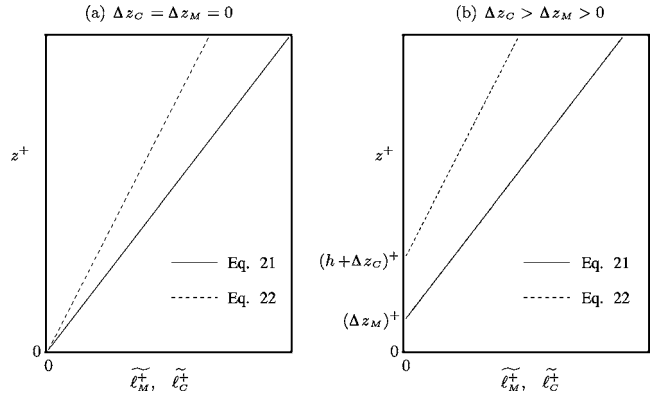

FIG. 6. Mixing length model for (a) $\Delta z_C = \Delta z_M = 0$ and (b) $\Delta z_C > \Delta z_M > 0$.

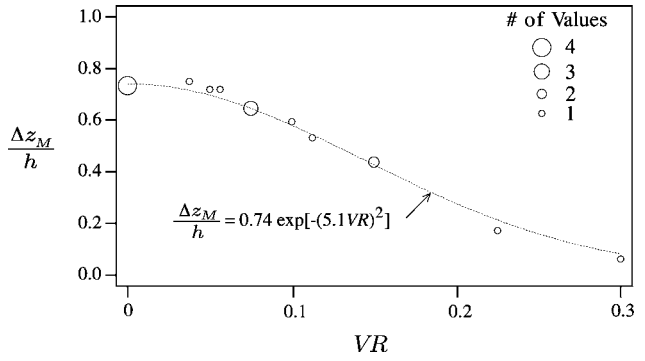

FIG. 8. Nondimensionalized momentum mixing length offsets, $\Delta z_M/h$, versus the normalized velocity ratio, VR. Circles are $\Delta z_M/h$ data (the symbol sizes reflect the number of Δz_M values calculated for the given value of VR, as defined in the figure). The dotted line is a least-squares empirical fit to the data.

To demonstrate the model, we first consider the simple case where $z_M = z_C = 0$, so that $\widetilde{\ell_M^+}$ and $\widetilde{\ell_C^+}$ have the same origins, and $\widetilde{\mathrm{Pr}_t} = \mathrm{Pr}_t$. This mixing length distribution is shown in Fig. 6(a), and the corresponding Pr_t distribution calculated with Eq. (19) is shown in Fig. 7(a). The Pr_t values are constant over the depth, and equal to $\widetilde{\mathrm{Pr}_t}$. However, when z_M and z_C are nonzero, a different behavior arises. Figure 6(b) shows the $\widetilde{\ell_M^+}$ and $\widetilde{\ell_C^+}$ distributions corresponding to the case where $\Delta z_C > \Delta z_M > 0$, and Fig. 7(b) shows the resulting $\widetilde{\mathrm{Pr}_t}$ distribution. Far from the wall ($z_C^+ \gg \Delta\ell^+$), Pr_t asymptotes to $\widetilde{\mathrm{Pr}_t}$, in agreement with the model results for Fig. 7(a). However, close to the wall, Pr_t grows large, becoming unbounded as z^+ approaches $(h+\Delta z_C)^+$. The large values of Pr_t close to the wall are simply due to the fact that the ℓ_M values are large relative to the ℓ_C values, due to the differing assumed origins for the two distributions. Note that values of Pr_t are not defined in the model for $z < (h+\Delta z_C)$, since ℓ_C is not defined there.

E. Experimental determination of Δz_M and Δz_C

We determined the coordinate offsets Δz_M and Δz_C using profiles of momentum and scalar mixing lengths calculated from measured velocity and scalar concentration data. Momentum mixing length distributions are calculated by combining Eqs. (10) and (3) into the form

$$\widetilde{\ell_M^+} = \frac{\left[-\sqrt{\overline{uw}}/\left(\partial U/\partial z\right)\right]^+}{\widetilde{D}(z^+,h^+)}, \tag{25}$$

where $\widetilde{D}$ is the damping factor given by Eq. (9). The parameter Δz_M is determined by plotting $\widetilde{\ell_M^+}$ vs z_M^+ and choosing the value of Δz_M that minimizes the error between the data calculated with Eq. (25) and the assumed linear distribution given by Eq. (10). Likewise, an equation for calculating scalar mixing length distributions can be formed by combining Eq. (25) with Eq. (11) to get

$$\widetilde{\ell_C^+} = \frac{\left\{-\overline{wc}/\left[\sqrt{-\overline{uw}}\left(\partial C/\partial z\right)\right]\right\}^+}{\widetilde{D}(z^+,h^+)}. \tag{26}$$

Then, $\widetilde{\ell_C^+}$ is plotted versus z_C^+, and Δz_C is again chosen to minimize the error between Eq. (26) and the assumed form given by Eq. (15). Because the assumed mixing length distributions given by Eqs. (10) and (15) are independent of the roughness Reynolds number, the approach for determining Δz_M and Δz_C can be used for any roughness regime (smooth, transitional, or fully rough).

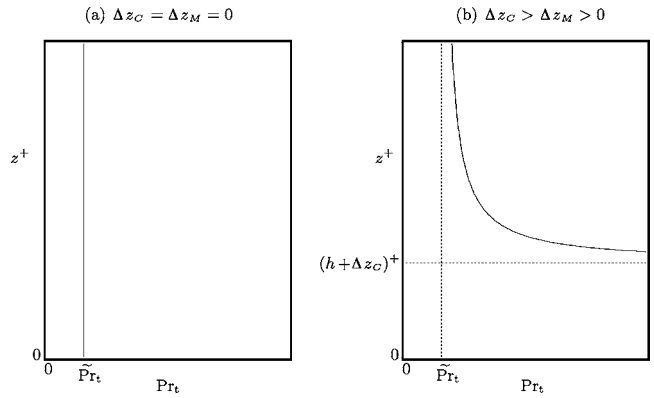

FIG. 7. Turbulent Prandtl number distributions calculated using Eq. (19) for the assumed mixing lengths shown in Fig. 6: (a) $\Delta z_C = \Delta z_M = 0$ and (b) $\Delta z_C > \Delta z_M > 0$.

IV. RESULTS

A. Mixing lengths

We now apply the analytical methodology developed in the previous section to experimental data acquired with the combined LDV/LIF probe over arrays of model clams with flush and raised siphons. The first step is to calculate momentum and scalar mixing lengths, and to use the resulting distributions to determine the mixing length offsets Δz_M and Δz_C.

The variation of Δz_M with VR for the raised siphon cases is shown in Fig. 8. The values of Δz_M are normalized by the siphon height h (see Fig. 5). The calculated Δz_M values are shown with symbols. Where more than one data point exists at a given VR value, the data are averaged to a single point;

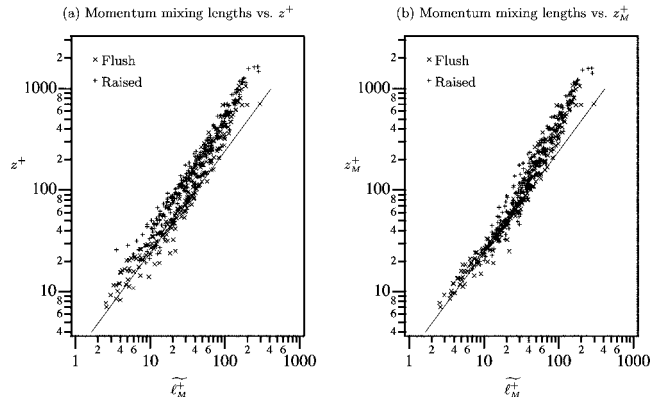

FIG. 9. Normalized momentum mixing lengths for all flow conditions plotted versus (a) z^+ and (b) z_M^+. Data from all 32 experimental cases (siphons flush and siphons raised) are shown. For the right-hand plot, Δz_M is chosen for each experimental case, such that the near-wall data match Eq. (21), which is shown in both plots by the solid line.

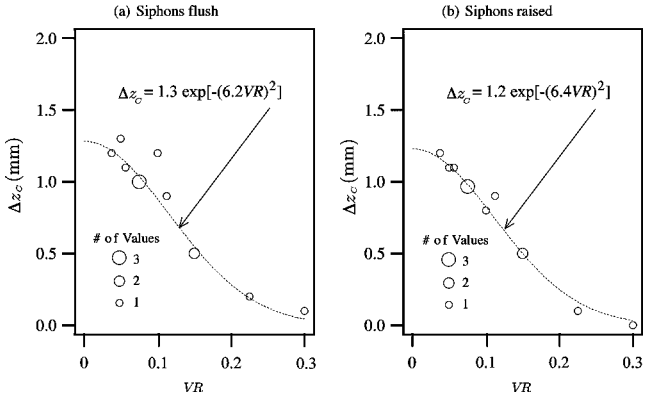

FIG. 10. Scalar mixing length offsets, Δz_C versus the normalized velocity ratio, VR. The symbols are Δz_C data (the symbol sizes reflect the number of Δz_C values calculated for the given value of VR). The dotted line is the proposed Δz_C model.

the size of the symbol indicates the number of data points averaged, as shown in the figure legend. The Δz_M offset data are well described by an empirical curve fit with exponential form, as shown in the figure. As VR$\rightarrow$0 (no siphonal pumping), the value of Δz_M asymptotes to $0.74h$. By definition, $z=\Delta z_M$ is the location where the extrapolated log law would give $U(z)=0$, and thus $\Delta z_M=0.74h$ is a measure of the roughness length[8] for $Q=0$. As VR increases, Δz_M decreases, indicating that the mixing length at a given height is increasing due to increased mixing by the siphonal pumping. For large VR values, the mixing length origin is depressed asymptotically toward the bed at $z=0$. No Δz_M results for the flush siphons are presented since these values were all essentially zero (within the positional accuracy of the LDV traverse).

Figure 9(a) shows calculated momentum mixing lengths, normalized as $\tilde{\ell}_M^+$, and plotted versus z^+ for all 32 experimental cases. As a reference, the flush-siphon and raised-siphon cases are indicated with × and + symbols, respectively. The straight line on the plot is Eq. (10), the assumed momentum mixing length distribution. Figure 9(b) shows the same data, except that it is now plotted versus z_M^+. Each of the experimental cases is assigned a Δz_M value that gives the best near-wall agreement with Eq. (10). The z_M^+ scaling is effective at producing a good near-wall fit, and removes the effect of siphon height (raised or flush) from the data. Far from the bed, the $\tilde{\ell}_M^+$ mixing lengths cease to grow as rapidly as in the assumed distribution.

The variation of Δz_C with VR for flush and raised siphons is shown in Figs. 10(a) and 10(b). The Δz_C offset (which is measured relative to the siphon tops), behaves similarly for the flush and raised siphons. In both cases, the scalar mixing length origin moves down toward the siphon tops as VR increases, meaning that the scalar mixing lengths are increasing at any fixed height in the flow. As before, the Δz_C offset data are well described by an empirical curve fit with exponential form, as shown in the figures.

Figure 11(a) shows calculated scalar mixing lengths, normalized as $\tilde{\ell}_C^+$, and plotted versus z^+ for the 24 experimental cases for which dye was present (i.e., excluding the eight $Q=0$ cases). In addition to being coded as before to indicate the siphon position, the plotted data are color coded according to the value of the velocity ratio VR. There is a significant amount of structure introduced by VR into the

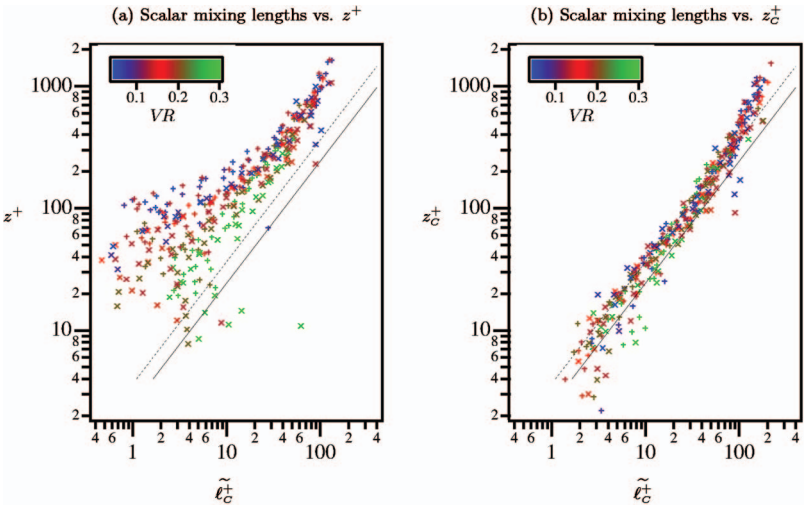

FIG. 11. (Color) Normalized scalar mixing lengths plotted versus (a) z^+ and (b) z_C^+. The solid line is Eq. (22) with $\widetilde{Pr}_t=1.0$, and the dotted line is Eq. (22) with $\widetilde{Pr}_t=1.5$. Symbols are the same as in Fig. 9.

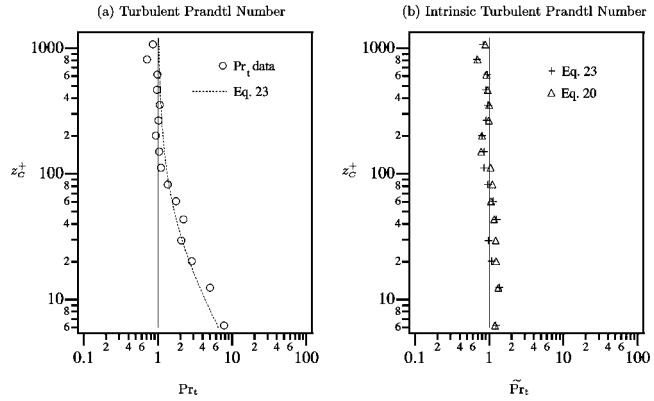

FIG. 12. $\mathrm{Pr_t}$ and $\widetilde{\mathrm{Pr_t}}$ calculations (siphons raised, $U_0=30$ cm/s, $Q=0.060$ ml/s).

near-wall distributions of $\widetilde{\ell_C^+}$. Two versions of Eq. (22) are shown in the figure: one for an assumed $\widetilde{\mathrm{Pr_t}}$ value of unity (solid line), and one for $\widetilde{\mathrm{Pr_t}}=1.5$ (dotted line). Figure 11(b) shows the scalar mixing lengths plotted versus z_C^+, which incorporates the offsets Δz_C. We found that the offsets could be best used to make the mixing lengths assume the form of Eq. (22) if a value of $\widetilde{\mathrm{Pr_t}}=1.5$ was used. The Reynolds analogy suggests that $\widetilde{\mathrm{Pr_t}}$ be on the order of unity, so a value of 1.5 is not unreasonable. Note that the z_C^+ scaling is effective at removing the structure associated with VR.

B. Turbulent Prandtl numbers

Having calculated scalar and momentum mixing length distributions and offsets in the previous section, we now use them to calculate turbulent Prandtl number distributions. For clarity, we begin by presenting results for a single experimental flow case (siphons raised, $U_0=30$ cm/s, $Q=0.060$ ml/s). Figure 12(a) shows $\mathrm{Pr_t}$ data values (symbols) calculated from Eqs. (18), (25), and (26), compared with the prediction from our analytical model (dotted line), calculated using Eq. (23) with $\widetilde{\mathrm{Pr_t}}=1.0$. Far from the bed, the $\mathrm{Pr_t}$ values are approximately unity. Closer to the bed ($z_C^+<100$), the $\mathrm{Pr_t}$ values grow monotonically. The model prediction (which is based on a $\Delta\ell$ value calculated from the mixing length data) is in good agreement with the data.

Figure 12(b) shows data from the same experimental case, but presented in terms of $\widetilde{\mathrm{Pr_t}}$ instead of $\mathrm{Pr_t}$. The + symbols are calculated using Eq. (23); namely, these data are the ratio of the symbols and the dotted line in Fig. 12(a). The triangle symbols are calculated using Eq. (20) by directly taking the ratio of the momentum and scalar mixing lengths, but from separate locations within the flow. The two approaches to calculating $\widetilde{\mathrm{Pr_t}}$ yield similar results. $\widetilde{\mathrm{Pr_t}}$ is approximately unity, but tends to be closer to 1.5 near the bed.

Figure 13 contains $\mathrm{Pr_t}$ and $\widetilde{\mathrm{Pr_t}}$ data from all 28 experimental cases with siphonal pumping. Figure 13(a) shows $\mathrm{Pr_t}$ plotted versus z^+, and the data are color coded by VR, as shown in the legend. The $\mathrm{Pr_t}$ data exhibit a strong structural dependence on VR, and the $\mathrm{Pr_t}$ values extend over a large range. When the data are recalculated in terms of $\widetilde{\mathrm{Pr_t}}$ [Fig. 13(b)], the dependence on VR is eliminated, and the $\widetilde{\mathrm{Pr_t}}$ values are all approximately unity (although closer to 1.5 near the bed). Figure 13(a) demonstrates that the traditional definition of $\mathrm{Pr_t}$ yields a wide range of values, depending on the experimental case and the distance from the bed. However, Fig. 13(b) demonstrates that a large portion of these variations can be captured using the turbulent Prandtl number model put forth in this paper.

V. SUMMARY AND DISCUSSION

The concept of a turbulent Prandtl number has historically used to denote the relative rates of mixing of a scalar and momentum. When these two mixing rates are expressed in terms of mixing lengths, the turbulent Prandtl number becomes equivalent to the ratio of the mixing lengths. In the case where the two assumed mixing length distributions have separate origins, the turbulent Prandtl number based on the mixing length ratio is influenced by two effects: the offset between the two origins and the difference in the growth rate of the two mixing length distributions. In this paper we proposed a model that explicitly separates these two effects. The ratio of the growth rates of the two distributions is termed the intrinsic turbulent Prandtl number [Eq. (19)]. We then pro-

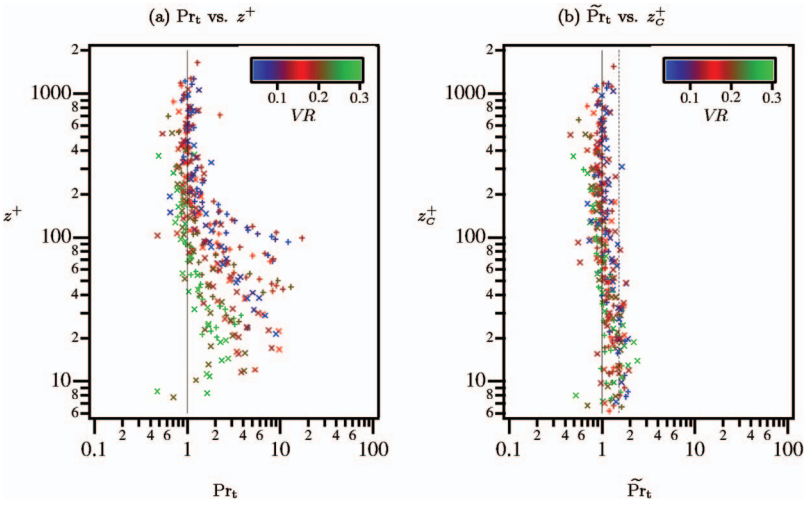

FIG. 13. (Color) Scatter plots for all flow cases for (a) $\mathrm{Pr_t}$ versus z^+ using Eq. (18) and (b) $\widetilde{\mathrm{Pr_t}}$ vs z_C^+ using Eq. (23). The solid line is $\widetilde{\mathrm{Pr_t}}=1.0$; the dotted line is $\widetilde{\mathrm{Pr_t}}=1.5$. The symbols are the same as in Fig. 9.

posed a model for predicting Pr_t based on $\widetilde{Pr}_t$ and the offset between the two origins [Eq. (23)]. Our results indicate that this model is effective at parametrizing Pr_t for the flume experiments over the model clams.

The technique relies on the ability to model the complex vertical distribution of momentum sink (roughness) and scalar source (dye injection) by discrete mixing length origins. This approach was successful for both the momentum (Fig. 9) and scalar (Fig. 11) mixing length distributions. The momentum mixing length offset is an effective roughness length scale, and it combines the effect of the "passive" bed roughness with the "active" siphon pumping. Thus, our results indicate that the complex siphon flows can be effectively modeled as an effective "active" roughness.

In many cases, it ought to be possible to estimate the mixing length offsets based purely on the known boundary conditions of the flow. Thus, the momentum offset would be estimated based on some fraction of the roughness scale, and the scalar offset would be based on knowledge of the scalar injection geometry. The model proposed in this paper then permits the vertical distribution of Pr_t to be predicted based only on these two estimates and an assumed value of $\widetilde{Pr}_t$ (presumably near unity). In the experimental case shown herein, Pr_t values grew large near the bed since the scalar origin lay above the momentum origin. If the opposite were true, then the near-bed values of Pr_t would be less than unity. In all cases, the model predicts that the farfield value of Pr_t approaches $\widetilde{Pr}_t$ since the flow can no longer distinguish between the two origins.

The measurement (and model prediction) in this study of Pr_t values that greatly exceed unity should not be viewed as being inconsistent with the Reynolds analogy. Instead, the model suggests that the Reynolds analogy is best applied to $\widetilde{Pr}_t$ rather than to Pr_t itself. The parameter $\widetilde{Pr}_t$ is a measure of the intrinsic relative ability of the local turbulence to transport momentum and scalars, and is expected to be order unity. The large deviations from unity in Pr_t can be predicted by the geometric and kinematic nature of the momentum and scalar boundary conditions.

ACKNOWLEDGMENTS

The authors gratefully acknowledge support from the National Science Foundation (Grant No. OCE950408). We are indebted to Peter Bradshaw for valuable discussions regarding this paper.

[1] A. J. Reynolds, "Prediction of turbulent Prandtl and Schmidt numbers," Int. J. Heat Mass Transfer **18**, 1055 (1975).
[2] W. M. Kays, "Turbulent Prandtl number—where are we," ASME J. Heat Transfer **116**, 284 (1994).
[3] G. P. Hammond, "Turbulent Prandtl number within a near-wall flow," AIAA J. **23**, 1668 (1985).
[4] R. A. Antonia and J. Kim, "Turbulent Prandtl number in the near-wall region of a turbulent channel flow," Int. J. Heat Mass Transfer **34**, 1905 (1991).
[5] B. M. Mitrovic and D. V. Papavassiliou, "Transport properties for turbulent dispersion from wall sources," AIChE J. **49**, 1095 (2003).
[6] D. Hollingsworth, W. Kays, and R. Moffat, "Measurement and prediction of the turbulent thermal boundary layer in water on flat and concave surfaces," Technical Report HMT-41, Thermosciences Division, Department of Mechanical Engineering, Stanford University, Stanford, CA, 1989.
[7] A. Snijders, A. Koppius, C. Nieuwvelt, and D. deVries, "An experimental determination of the turbulent Prandtl number in the inner boundary layer for an air flow over a flat plate," in 6th International Heat Transfer Conference, Toronto, Canada, 1978, Vol. 2, pp. 519–523.
[8] M. Raupach, R. Antonia, and S. Rajagopalan, "Rough-wall turbulent boundary layers," Appl. Mech. Rev. **44**, 1 (1991).
[9] B. J. Belnap, J. A. van Rij, and P. M. Ligrani, "A Reynolds analogy for real component surface roughness," Int. J. Heat Mass Transfer **45**, 3089 (2002).
[10] J. Cloern, "Does the benthos control phytoplankton biomass in South San Francisco Bay?" Mar. Ecol.: Prog. Ser. **9**, 191 (1982).
[11] J. Crimaldi, "Turbulence structure of velocity and scalar fields over a bed of model bivalves," Ph.D. thesis, Stanford University, 1998.
[12] P. Spalart, "Direct simulation of a turbulent boundary layer up to $Re_{\delta_2}=1410$," J. Fluid Mech. **187**, 61 (1988).
[13] C. O'Riordan, S. Monismith, and J. Koseff, "A study of concentration boundary-layer formation over a bed of model bivalves," Limnol. Oceanogr. **38**, 1712 (1993).
[14] C. O'Riordan, S. Monismith, and J. Koseff, "The effect of bivalve excurrent jet dynamics on mass transfer in a benthic boundary layer," Limnol. Oceanogr. **40**, 330 (1995).
[15] S. Monismith, J. Koseff, J. Thompson, C. O'Riordan, and H. Nepf, "A study of model bivalve siphonal currents," Limnol. Oceanogr. **35**, 680 (1990).
[16] F. Durst and F. Schmitt, "Joint laser-Doppler/laser-induced fluorescence measurements in a turbulent jet," in Proceedings of the 2nd Symposium on Applications of Laser Anemometry to Fluid Mechanics, 1984.
[17] M.-C. Lai and G. Faeth, "A combined laser-Doppler anemometer/laser-induced fluorescence system for turbulent transport measurements," Trans. ASME, Ser. C: J. Heat Transfer **109**, 254 (1987).
[18] F. Lemoine, Y. Antoine, M. Wolff, and M. Lebouche, "Simultaneous temperature and 2d velocity measurements in a turbulent heated jet using combined laser-induced fluorescence and LDA," Exp. Fluids **26**, 315 (1999).
[19] P. N. Papanicolaou and E. J. List, "Investigations of round vertical turbulent buoyant jets," J. Fluid Mech. **195**, 341 (1988).
[20] J. Crimaldi, "The effect of photobleaching and velocity fluctuations on single-point LIF measurements," Exp. Fluids **23**, 325 (1997).
[21] E. Van Driest, "On turbulent flow near a wall," J. Aeronaut. Sci. **23**, 1007 (1956).